

---

This is an electronic reprint of the original article.

This reprint may differ from the original in pagination and typographic detail.

Lin, Qiaoling; Fang, Hanlin; Kalaboukhov, Alexei; Liu, Yuanda; Zhang, Yi; Fischer, Moritz; Li, Juntao; Hagel, Joakim; Brem, Samuel; Malic, Ermin; Stenger, Nicolas; Sun, Zhipei; Wubs, Martijn; Xiao, Sanshui

**Moiré-engineered light-matter interactions in  $\text{MoS}_2/\text{WSe}_2$  heterobilayers at room temperature**

*Published in:*  
Nature Communications

*DOI:*  
[10.1038/s41467-024-53083-x](https://doi.org/10.1038/s41467-024-53083-x)

Published: 01/12/2024

*Document Version*  
Publisher's PDF, also known as Version of record

*Published under the following license:*  
CC BY-NC-ND


*Please cite the original version:*  
Lin, Q., Fang, H., Kalaboukhov, A., Liu, Y., Zhang, Y., Fischer, M., Li, J., Hagel, J., Brem, S., Malic, E., Stenger, N., Sun, Z., Wubs, M., & Xiao, S. (2024). Moiré-engineered light-matter interactions in  $\text{MoS}_2/\text{WSe}_2$  heterobilayers at room temperature. *Nature Communications*, 15(1), Article 8762.  
<https://doi.org/10.1038/s41467-024-53083-x>

# Moiré-engineered light-matter interactions in MoS<sub>2</sub>/WSe<sub>2</sub> heterobilayers at room temperature

Received: 10 April 2024

Accepted: 26 September 2024

Published online: 09 October 2024

 Check for updates

Qiaoling Lin<sup>1,2,3,10</sup>, Hanlin Fang<sup>1,2,4,10</sup> , Alexei Kalaboukhov<sup>4</sup>, Yuanda Liu<sup>5</sup>, Yi Zhang<sup>6</sup>, Moritz Fischer<sup>1,2,3</sup>, Juntao Li<sup>7</sup>, Joakim Hagel<sup>8</sup>, Samuel Brem<sup>9</sup>, Ermin Malic<sup>9</sup>, Nicolas Stenger<sup>1,2,3</sup>, Zhipei Sun<sup>6</sup>, Martijn Wubs<sup>1,2,3</sup> & Sanshui Xiao<sup>1,2,3</sup> 

Moiré superlattices in van der Waals heterostructures represent a highly tunable quantum system, attracting substantial interest in both many-body physics and device applications. However, the influence of the moiré potential on light-matter interactions at room temperature has remained largely unexplored. In our study, we demonstrate that the moiré potential in MoS<sub>2</sub>/WSe<sub>2</sub> heterobilayers facilitates the localization of interlayer exciton (IX) at room temperature. By performing reflection contrast spectroscopy, we demonstrate the importance of atomic reconstruction in modifying intralayer excitons, supported by the atomic force microscopy experiment. When decreasing the twist angle, we observe that the IX lifetime becomes longer and light emission gets enhanced, indicating that non-radiative decay channels such as defects are suppressed by the moiré potential. Moreover, through the integration of moiré superlattices with silicon single-mode cavities, we find that the devices employing moiré-trapped IXs exhibit a significantly lower threshold, one order of magnitude smaller compared to the device utilizing delocalized IXs. These findings not only encourage the exploration of many-body physics in moiré superlattices at elevated temperatures but also pave the way for leveraging these artificial quantum materials in photonic and optoelectronic applications.

Moiré superlattices formed with monolayers of two-dimensional (2D) materials offer a new degree of freedom (moiré lattice constant or moiré period) for manipulating electronic band structure<sup>1–3</sup>. The moiré period can be efficiently tuned by the twist angle and lattice mismatch between monolayers. Such a platform has been demonstrated to be

powerful in studying complex many-body physics owing to its excellent dynamical tunability with external controls (e.g., electric field and electrostatic doping)<sup>1</sup>. Beyond fundamental interests, moiré superlattices have been used to develop a low-power moiré synaptic transistor at room temperature<sup>4</sup>. An exemplary moiré superlattice is twisted

<sup>1</sup>Department of Electrical and Photonics Engineering, Technical University of Denmark, DK-2800 Kongens Lyngby, Denmark. <sup>2</sup>NanoPhoton - Center for Nanophotonics, Technical University of Denmark, DK-2800 Kongens Lyngby, Denmark. <sup>3</sup>Centre for Nanostructured Graphene, Technical University of Denmark, DK-2800 Kongens Lyngby, Denmark. <sup>4</sup>Department of Microtechnology and Nanoscience (MC2), Chalmers University of Technology, 41296 Gothenburg, Sweden. <sup>5</sup>Institute of Materials Research and Engineering, Agency for Science Technology and Research (A\*STAR), 2 Fusionopolis Way, 138634 Singapore, Singapore. <sup>6</sup>Department of Electronics and Nanoengineering and QTF Centre of Excellence, Aalto University, Espoo 02150, Finland. <sup>7</sup>State Key Laboratory of Optoelectronic Materials and Technologies, School of Physics, Sun Yat-Sen University, Guangzhou 510275, China. <sup>8</sup>Department of Physics, Chalmers University of Technology, 41296 Gothenburg, Sweden. <sup>9</sup>Department of Physics, Philipps-Universität Marburg, 35037 Marburg, Germany. <sup>10</sup>These authors contributed equally: Qiaoling Lin, Hanlin Fang. ✉e-mail: [hanfan@dtu.dk](mailto:hanfan@dtu.dk); [saxi@dtu.dk](mailto:saxi@dtu.dk)

bilayer graphene with a magic twist angle of  $-1.1^\circ$ , where flat bands are predicted<sup>5</sup> and contributed to a tunable unconventional superconductivity with electrostatic doping<sup>6</sup>. Unlike graphene without a band gap, semiconducting transition metal dichalcogenides (TMDs) offer a wide range of band gaps, paving the way to photonic and optoelectronic applications<sup>7</sup>. Moreover, the band structure of 2D-TMDs can be engineered by stacking different TMD monolayers with type-II band alignment<sup>8</sup>, offering opportunities for light emission at various wavelength windows. Interlayer excitons (IXs) in TMD heterobilayers dominate the light emission properties of the material at room temperature due to the large binding energies ( $>100$  meV)<sup>9</sup>. The spatially separated electron-hole pair leads to long-lived IX (on the order of nanoseconds), which is advantageous for low threshold lasing<sup>10–12</sup>.

Atomic reconstruction occurs when the twist angle is small (depending on the materials), meaning that the constituent monolayers cannot be treated as rigid lattices. The resulting reconstruction of the moiré pattern can be visualized by various imaging techniques, including transmission electron microscopy (TEM) and atomic force microscopy (AFM)<sup>13</sup>. The topological pattern as a consequence of a periodically modulated strain distribution in moiré superlattices regulates the interaction of carriers and promotes exciton localization in moiré potentials<sup>14–16</sup>. The moiré-trapped IXs in TMD heterobilayers are predicted to be a 2D array of quantum emitters<sup>17</sup>. They were first observed by far-field optical spectroscopy at cryogenic temperatures<sup>18–21</sup>, and further visualized in momentum space by photoemission spectroscopy<sup>22,23</sup> and in real space by cryogenic TEM<sup>15</sup>. However, the study of exciton physics in moiré superlattices has been limited to impractically low temperatures, and the application of moiré-trapped excitons on light-emitting devices at room temperature is unexplored.

In this work, we observe multiple IX peaks in the photoluminescence (PL) spectrum of  $\text{MoS}_2/\text{WSe}_2$  heterobilayers with small twist angles ( $-0.5^\circ$ ). Additionally, the lowest-energy IX state shows significant saturation behavior with increasing pump power, indicating the exciton localization arising from moiré potential at room temperature. By performing reflection contrast (RC) spectroscopy, we observe that the  $\text{MoS}_2$  A-exciton energy in the moiré superlattices is lower than that in bilayer  $\text{MoS}_2$ . This feature is associated with atomic reconstruction (characterized as the periodically modulated height profile in an AFM image) that contributes to the localization of excitons. The brighter IX with a longer exciton lifetime with decreasing twist angle indicates that the moiré potential plays an important role in suppressing non-radiative channels. To explore the importance of the moiré-trapped IXs for light-emitting devices, heterobilayers with small twist angles are then integrated with silicon single-mode cavities. We discover that moiré-trapped IXs make devices with thresholds one order of magnitude lower than when using delocalized IXs.

## Results

### Localized interlayer excitons at room temperature

The investigated  $\text{MoS}_2/\text{WSe}_2$  heterobilayers are fabricated by the dry transfer technique (details in Methods) to obtain a clean interface, as evidenced by the strongly quenched PL of intralayer excitons (Fig. S1). An IX is formed after a fast charge transfer process<sup>24,25</sup> and its energy is well below the A-exciton energy of  $\text{MoS}_2$  and  $\text{WSe}_2$  due to the large band offset of the monolayers (see inset of Fig. 1a). It has been reported that the moiré potential formed in  $\text{MoS}_2/\text{WSe}_2$  heterobilayers with a small twist angle ( $\theta$ ) can confine IXs at cryogenic temperatures<sup>26</sup> (see Fig. 1a for a sketch). When the temperature increases, moiré-trapped IXs usually become delocalized after phonon scattering and dielectric screening, especially at room temperature<sup>27</sup>.

Here we focus on examining the exciton localization with moiré potential at room temperature, and all our measurements are performed at this temperature. We use a continuous wave (CW) laser with an energy of 1.938 eV and a power of 33.5  $\mu\text{W}$  to excite samples with

different twist angles, and the measured PL spectra are displayed in Fig. 1b. The PL emission energies cover a spectral range from 0.95 – 1.15 eV, which are consistent with the reported K-K transition energies of  $\text{MoS}_2/\text{WSe}_2$  heterobilayers<sup>28,29</sup> and thus indicate the origin of the direct bandgap of our samples. Additionally, we observe that the spectral profile of the PL peaks changes from a non-symmetric peak with a low-energy tail (the blue curve) to a non-symmetric peak with a high-energy tail (the red curve) upon decreasing the twist angle. This transformation reflects the change of the dominant mechanism modulating the PL spectra, which are discussed in Note S1.

To examine the effectiveness of moiré potential in the samples with a small twist angle ( $-0.5^\circ$ ), we perform power-dependent measurements (see Fig. 1c). With the lowest pump power, only one peak is visible in the PL spectrum. When the pump power increases, two additional higher-energy peaks appear. These three peaks are denoted as IX1 ( $-0.968$  eV), IX2 ( $-1.009$  eV), and IX3 ( $-1.038$  eV), respectively. Figure 1d shows that the PL intensities of IX1 and IX2 saturate with increasing pump power while that of IX3 increases linearly, revealing that IX1 and IX2 are localized states while IX3 is a delocalized state<sup>30,31</sup>. That is, excitons have the largest occupation possibility in the ground state at low pump power, and then the occupation possibility of higher energy states increases upon pump power. Such an exciton-filling effect agrees well with the previous reports about excitons confined within moiré potential traps<sup>18,31</sup>. Provided that IX1 and IX2 originate from different potential traps, we would expect to observe the PL emission from IX1 and IX2 since the lowest applied pump power, like the observation of defect-related states in the previous report<sup>31</sup>. Therefore, we expect that IX1 and IX2 originate from the same potential trap (see the inset of Fig. 1d). In stark contrast, no multi-peaks feature and no saturation behavior with pump power are found in the  $-2.8^\circ$  heterobilayer (Fig. S2). This twist-angle-dependence helps us to rule out the contribution of disorder in the materials.

The remarkable blueshift of IX1 with pump power (see Fig. 1c) manifests a strong dipole-dipole repulsion enabled by the strong exciton confinement<sup>32,33</sup>, allowing us to find that the exciton density at the maximum applied pump power is below the moiré density (see Note S2). Moreover, the moiré period of 8.4 nm (see Fig. 1e and Note S3) of the  $-0.5^\circ$   $\text{MoS}_2/\text{WSe}_2$  heterobilayer is larger than the measured diameter of IX of  $\sim 5.2$  nm<sup>22</sup>, permitting the exciton confinement. Therefore, we conclude that IX1 and IX2 originate from moiré potential-trapped states. To study the angle-dependent IX energy systematically, we prepare more samples and their PL peak energy versus twist angle is shown in Fig. 1e. It is worth noting that the multi-peaks feature is only visible for samples with a twist angle of  $-0.5^\circ$ , and thus the PL peak energy cannot be assigned to a specific excitonic state. The data is fitted well by an exponential function, which will be used to estimate the twist angle (see Note S4). We notice that the energy shift ( $\sim 200$  meV) is about four times larger than those reported in other moiré superlattices<sup>21,34</sup>, implying the presence of a deeper moiré potential trap in our fabricated samples.

### Features of intralayer excitons in moiré superlattices

To further explore the nature of the emergent moiré-trapped IX at room temperature, we characterize the intralayer exciton resonances using RC spectroscopy. Figure 2a displays the RC spectra of different twisted  $\text{MoS}_2/\text{WSe}_2$  heterobilayers, uncoupled bilayer (2L)  $\text{MoS}_2/\text{WSe}_2$ , and monolayers. The coupling in the heterostructures can be characterized by the PL quenching (see Fig. S1) and energy shift (see Fig. 2a) of  $\text{WSe}_2$  excitons. The RC spectrum of IX is not shown here due to its orders of magnitude smaller oscillator strength<sup>35</sup>. Intralayer excitons in monolayer  $\text{WSe}_2$ , monolayer  $\text{MoS}_2$ , and 2L- $\text{MoS}_2$  are marked by blue dashed, red dashed, and green dashed lines, respectively. Intralayer excitons in  $\text{WSe}_2$  and  $\text{MoS}_2$  show significantly different twist angle dependence. Their energies are extracted and plotted as a function of twist angle, as shown in Fig. 2b, c, respectively. We note that the twist

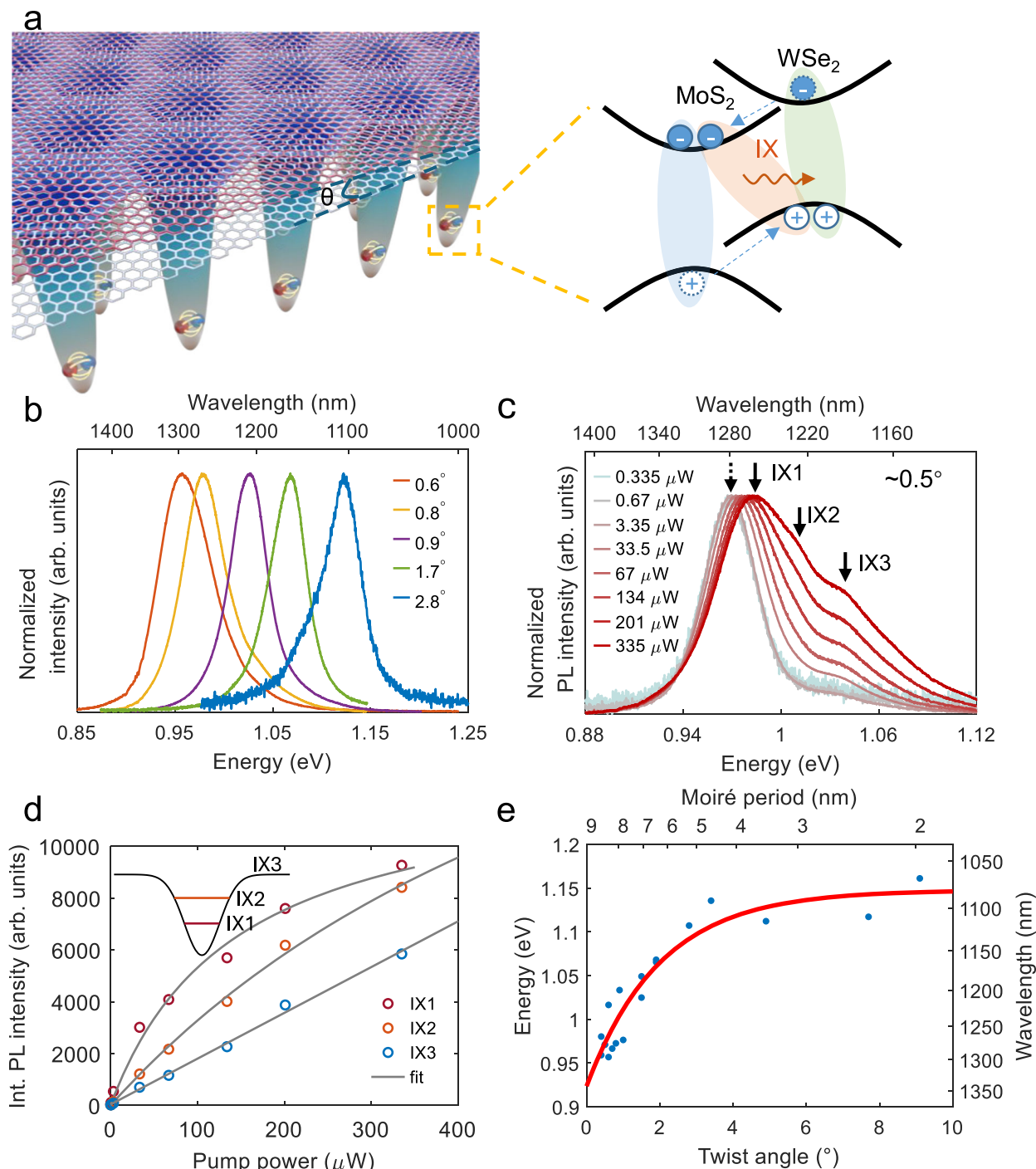


**Fig. 1 | Observation of moiré-trapped IX states in  $\text{MoS}_2/\text{WSe}_2$  heterobilayers.** **a** Schematic of IXs trapped in moiré potentials, where  $\theta$  is the twist angle between monolayers. The inset shows the band diagram of  $\text{MoS}_2/\text{WSe}_2$  heterobilayer at K valley and the formation of IXs. **b** The normalized PL spectra of different twisted samples. **c** Power-dependent PL spectra of a  $-0.5^\circ$   $\text{MoS}_2/\text{WSe}_2$  heterobilayer. The black arrows mark the multiple emission peaks originating from different IX states.

**d** The integrated PL intensity of the different IX states as a function of power with an integrated spectral range of 0.43 meV. The data of IX1 and IX2 are fitted with the formula  $I = I_{\text{max}} / (1 + P_{\text{sat}}/P)$ , where  $P_{\text{sat}}$  is the saturation power. The saturation power for IX1 and IX2 are  $144 \mu\text{W}$  and  $714 \mu\text{W}$ , respectively. The data of IX3 is fitted with a linear equation. **e** IX emission peak energy versus twist angle. The data is fitted by an exponential function.

angle is derived from the exponential fitting curve shown in Fig. 1c (see also Note S4).

For the twist angle changing from  $2.1^\circ$  to  $1.3^\circ$ ,  $X_{\text{WSe}_2}^A$  blueshifts, while  $X_{\text{MoS}_2}^A$  continuously redshifts. The lattice constant and interlayer spacing are the two geometrical parameters that have the greatest impact on exciton energy<sup>36</sup>. 2L- $\text{MoS}_2$  is a naturally favorable configuration where the interlayer coupling is very strong, as manifested by

the crossover from a direct bandgap of the monolayer to an indirect bandgap of the bilayer. The direct bandgap of  $\text{MoS}_2/\text{WSe}_2$  heterobilayers reveals a weaker interlayer coupling than 2L- $\text{MoS}_2$ . Therefore, the energy of  $X_{\text{MoS}_2}^A$  in the  $\text{MoS}_2/\text{WSe}_2$  should be located between the energy for the monolayer (the red dashed line) and bilayer  $\text{MoS}_2$  (the green dashed line). Surprisingly, Fig. 2c shows that the energies of  $X_{\text{MoS}_2}^A$  in  $\text{MoS}_2/\text{WSe}_2$  heterobilayers are below that in 2L- $\text{MoS}_2$ ,

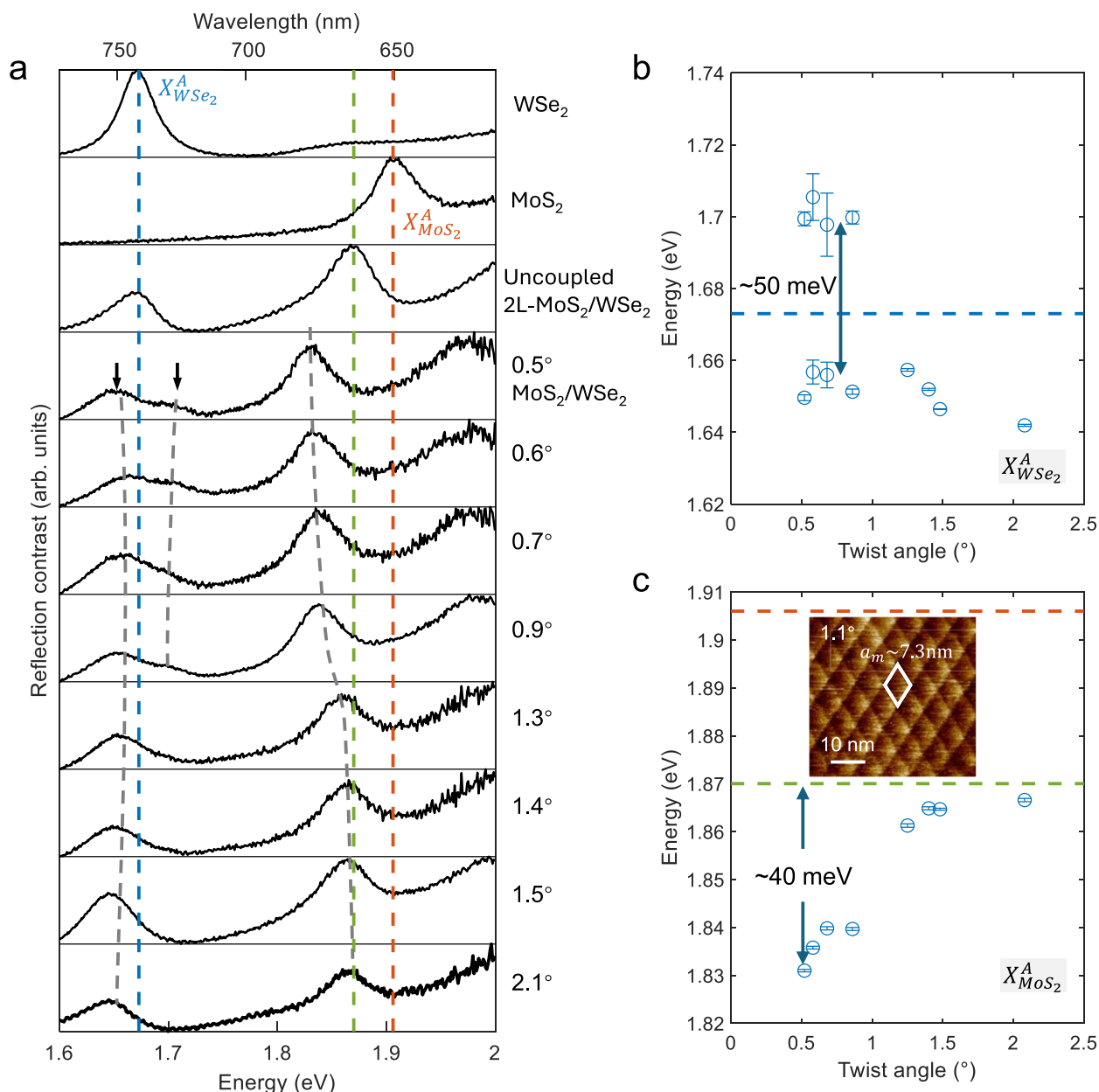


**Fig. 2 | Twist-angle dependent intralayer excitons.** **a** Evolution of RC spectra with twist angles. Intralayer excitons in WSe<sub>2</sub> and MoS<sub>2</sub> are denoted as  $X_{WSe_2}^A$  (blue-coded) and  $X_{MoS_2}^A$  (red-coded), respectively. Intralayer excitons of bilayer MoS<sub>2</sub> in an uncoupled 2L-MoS<sub>2</sub>/WSe<sub>2</sub> heterostructure (green-coded) are used as a reference to describe the energy shift of the intralayer exciton resonance. The curves are

shifted vertically for clarity, and the gray dashed lines are a guide to the eye. Panels **(b)** and **(c)** show the fitted exciton energy of WSe<sub>2</sub> and MoS<sub>2</sub> from **(a)** as a function of twist angle, respectively. The inset of **(c)** shows the AFM image of the periodically modulated height profile of a 1.1° MoS<sub>2</sub>/WSe<sub>2</sub> heterobilayer, and the amplitude of the height modulation is about 157 pm.

indicating that the significant redshift of  $X_{MoS_2}^A$  in twisted heterobilayers is not associated with the modulated interlayer coupling but the expanded lattice constant. Moreover, the energy difference increases to ~40 meV when the twist angle decreases to 0.5°, equivalent to a ~0.444% biaxial strain (considering a strain tunability of 90 meV/%<sup>37</sup>). Thus, the blueshift of  $X_{WSe_2}^A$  can be attributed to the compressive strain in the constituent monolayer WSe<sub>2</sub>. This opposite type of strain in the different monolayers indicates the appearance of atomic reconstruction<sup>38</sup>, instead of global strain induced by fabrication processes. In this case, monolayer WSe<sub>2</sub> with a larger lattice constant (0.328 nm) shrinks while monolayer MoS<sub>2</sub> with a smaller lattice constant (0.316 nm) expands.

To gain insight into the atomic reconstruction, we conduct AFM experiments. The inset of Fig. 2c shows the periodically modulated

height profile of a 1.1° MoS<sub>2</sub>/WSe<sub>2</sub> heterobilayer, confirming the presence of atomic reconstruction. This moiré pattern is usually not visible owing to a height modulation amplitude below the AFM resolution<sup>39,40</sup>. The apparent moiré pattern in our case is ascribed to the large lattice mismatch ( $\delta \sim 3.7\%$ ) of the constituent monolayers, resulting in a significant out-of-plane strain distribution. Additionally, we observe a clearer moiré pattern in another channel (see Fig. S3), indicating that the mechanical properties of the material are periodically altered. We note that the moiré pattern in the height channel is chosen because it directly manifests that the constituent monolayers cannot be treated as rigid lattices, i.e., atomic reconstruction happens. The imaged moiré cells consist of moiré domains and moiré domain walls that form potential traps that may capture excitons. The observed significant accumulated strain with decreasing twist angle reflects the



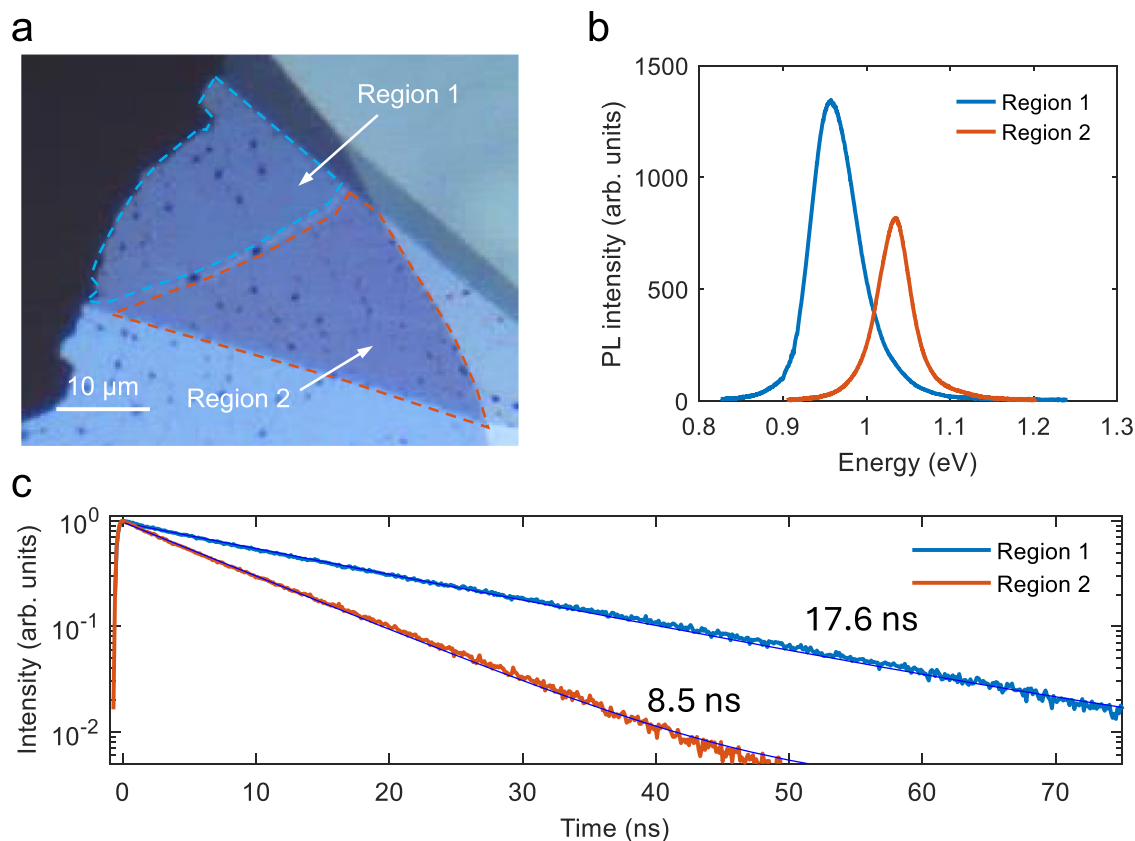


**Fig. 3 | Observation of moiré-prolonged exciton lifetimes.** **a** Optical microscope image of MoS<sub>2</sub>/WS<sub>2</sub> heterobilayer with two different twisted regions. **b** PL spectrum of the different twisted regions under the same pump power. **c** Time-resolved

PL dynamics from the two regions with different twist angles. The blue curves are exponential fits to the data, giving an IX lifetime of 17.6 ns (8.5 ns) for Region 1 (Region 2).

contribution of atomic reconstruction to the deepening of potential traps by increasing the lattice constant difference between the domains and domain walls<sup>39</sup>. The combined effect of atomic reconstruction and moiré pattern possibly accounts for the presence of localized excitons observed in Fig. 1c. When the twist angles are below 0.9° (see Fig. 2a), we can resolve an additional higher-energy state. This feature is commonly used to indicate intralayer excitons localized at the different sites of a moiré cell<sup>19</sup>. The splitting energy (~50 meV) of the two states is similar to the previous observation<sup>22</sup>. The absence of splitting of the MoS<sub>2</sub> exciton has remained unclear and needs further work. The higher-resolution imaging techniques such as hyperspectral imaging with a high-energy electron beam<sup>15</sup> could possibly provide the answer, however, it is beyond the scope of this work. Further, the moiré pattern becomes invisible in the ~4.4° twisted sample (Fig. S4), revealing the decreased height modulation with increased twist angle and ruling out the influence of measurement artifacts.

### Engineering exciton lifetimes with moiré potentials

Exciton lifetime engineering is crucial because it enables the precise control of light emission and energy transfer processes, which are fundamental for optimizing the performance of optoelectronic devices such as lasers<sup>10,41</sup>, and exciton condensation<sup>42</sup>. To study the significance of the moiré potentials on IX lifetime, different twisted samples are fabricated in the same way and characterized by time-resolved PL measurements (see Methods). However, we find that they do not show a clear trend of angle-dependent exciton lifetime (see Fig. S5), which is ascribed to the different optical quality of the samples resulting from material defect density or fabrication introduced imperfections. To eliminate the sample quality difference, we choose a sample (see Fig. 3a) consisting of two different twisted regions (Region 1 and Region 2 with

twist angles of ~0.3° and ~1.4° respectively) that are divided by a wrinkle (more discussion in Note S4). Region 1 with a smaller twist angle (manifested as lower emission energy) shows brighter PL emission intensity (see Fig. 3b) and a two times larger exciton lifetime (~17.6 ns, see Fig. 3c). We note that this trend is also observed in another similar sample (Fig. S6). This feature cannot be explained by the reduced momentum mismatch that typically leads to a shorter exciton lifetime<sup>43</sup>, which is the opposite of the observed trend in Fig. 3.

The brightness of a light emitter is related to its radiative and non-radiative lifetimes. A longer exciton lifetime generally gives rise to a weaker PL emission when the non-radiative effect is negligible, which is opposite to our observations. This inconsistency indicates that non-radiative centers such as defects play an important role in capturing excitons, thereby shortening IX lifetime (see more discussion in Note S5). Moreover, we find that the exciton lifetime of the lowest energy IX state does not decrease with increased pump power (Fig. S7), indicating that the protection of moiré trapping against exciton-exciton annihilation that can result in a shorter lifetime upon increasing pump power<sup>44</sup>. The suppression of exciton transport to non-radiative centers by the moiré potential accounts for the longer exciton lifetime in the smaller twisted moiré superlattice, similar to the observation of prolonged exciton lifetime in TMD monolayers after the passivation of defects<sup>45</sup>. These findings reflect that the IX lifetime at room temperature is limited by the sample quality, which is also supported by the observation of a significantly longer IX lifetime (~2 μs) at 4.5 K<sup>26</sup> where non-radiative recombinations are strongly suppressed.

### Coupling moiré superlattices to optical cavities

To explore the potential of the moiré-trapped IXs for photonic applications, small twisted (~0.5°) heterobilayers are integrated with silicon

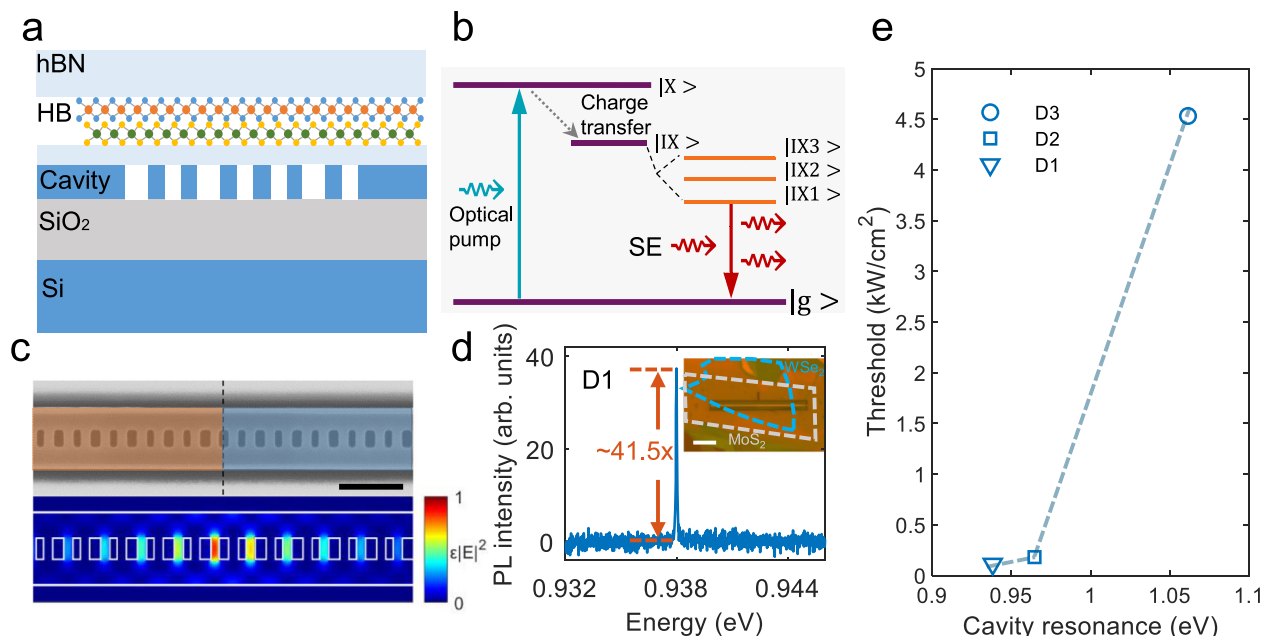


**Fig. 4 | Light emission with moiré superlattice-cavity devices.** **a** Sketch of the hBN-encapsulated MoS<sub>2</sub>/WSe<sub>2</sub> heterobilayer (HB) on a SiO<sub>2</sub>-supported silicon topological nanobeam cavity. **b** Energy level diagram of the moiré superlattice with a small twist angle. Spontaneous emission (SE) from IXs can be enhanced by a cavity. **c** SEM image (the upper panel) of the cavity. The light red and blue areas

illustrate two photonic crystals with different topological phases, leading to strong light confinement at their interface. The simulated mode profile is illustrated in the lower panel. Scale bar, 500 nm. **d** Output spectrum of device D1. The inset shows the optical microscope image of the device. Scale bar, 5  $\mu$ m. **e** The thresholds of devices D1, D2, and D3. The dashed lines are a guide to the eye.

topological cavities (see Fig. 4a for a sketch of the device). The heterobilayers are encapsulated within two hBN flakes to prevent optical performance degradation in ambient environments<sup>46</sup> and to suppress inhomogeneous linewidth broadening<sup>18</sup>. In this case, we also observe a clear multipeak feature in the PL spectrum (Fig. S8), again indicating the presence of the moiré effect. We note that photonic topological cavities are chosen due to their demonstrated robust single-mode operation<sup>47,48</sup>, preventing cavity mode competition, thus simplifying the study of the IX-cavity interaction. The top panel in Fig. 4c shows the scanning electron microscopy (SEM) image of our fabricated cavity, and the simulated electric-energy distribution shown in the bottom panel reflects that photons are well-confined around the interface between two photonic crystals with distinct topological phases<sup>48</sup>. In this scenario, the light enhancement can be qualitatively described by an equivalent three-level system (see Fig. 4b) that takes the above-mentioned multiple IX states ( $|IX1\rangle$ ,  $|IX2\rangle$ , and  $|IX3\rangle$ ) into account. The fast dissociation of the intralayer exciton state  $|X\rangle$  and long-lived IX state ( $|IX\rangle$ ) are beneficial for realizing population inversion.

We design and fabricate three representative devices (D1, D2, and D3) with optical cavity resonances that are mainly coupled to three different IX states ( $|IX1\rangle$ ,  $|IX2\rangle$ , and  $|IX3\rangle$ ) (see Fig. S9), respectively. Unlike the strong absorption of intralayer excitons that results in the disappearance of a cavity mode (see Fig. S10), all the moiré superlattice-cavity devices show a clear cavity mode and their cavity modes become dominant at different excitation densities (see Fig. S9). Figure 4d presents a pronounced cavity mode of D1 in the technologically important optical fiber communication O-band (1260–1360 nm or 0.912–0.984 eV), which is enabled by the moiré effect pushing IX energy into this range. A PL enhancement factor of ~41.5 times is observed with the help of a single-mode cavity (see more discussion in Note S6 and the comparison of the PL spectrum of on- and off-cavity in Fig. S11), which is remarkably larger than that of D3. This difference manifests the significance of moiré effects. Moreover, the measured emission linewidth of ~0.1 nm is limited by the spectral resolution of

our detection setup and yields the highest spectral purity compared to the reported 2D material lasers<sup>49</sup>.

Through power-dependent PL measurements, a light-in-light-out (L-L) curve is acquired to extract the threshold of the devices (Fig. S12), and the values are shown in Fig. 4e. It is clear that D1 has the lowest threshold of ~0.11 kW/cm<sup>2</sup>. In D2 where the cavity mode is also coupled to the moiré-localized IX shows a slightly higher threshold (~0.18 kW/cm<sup>2</sup>). In stark contrast, in D3, where the cavity mode is coupled to a delocalized IX state, it yields one order of magnitude higher threshold (~4.53 kW/cm<sup>2</sup>). This threshold value is close to that reported for a laser using delocalized IX<sup>10</sup>. Therefore, the significant difference in the threshold value of the three devices highlights the advantage of the moiré effect for energy-efficient light-emitting devices. It is worth noting that threshold behavior is commonly used as one of the indicators for the onset of lasing. However, the cavity-enhanced spontaneous emission can also show similar threshold behavior<sup>50</sup>. The conclusive demonstration of lasing-dominated emission thus requires the measurement of photon statistics by the Hanbury Brown and Twiss (HBT) experiment (Note S6). In our case, the weak output intensity prevents us from examining the lasing behavior.

## Discussion

In summary, our work clearly demonstrates the moiré effect in MoS<sub>2</sub>/WSe<sub>2</sub> heterobilayers at room temperature and its positive impact on supplying optical gain at low pump levels in the O-band. This encourages studies on many-body physics at elevated temperatures and offers a new architecture for integrated light sources for silicon photonics. The enhanced PL emission and prolonged exciton lifetime in moiré superlattices suggest that the device performance is mainly limited by the optical quality of moiré superlattices. We believe that further improvement in the material quality will pave the way to high-performance moiré photonic devices. Furthermore, a new technique that can directly map the excitonic gain in moiré superlattices and a more detailed theory of these moiré superlattice-cavity structures are

crucial for further advancing on-chip light sources, calling for further study.

## Methods

### Sample fabrication

MoS<sub>2</sub> and WSe<sub>2</sub> monolayers were prepared on a polydimethylsiloxane (PDMS) stamp by using Nitto tape to exfoliate flux-grown bulk crystals (2D semiconductors)<sup>51</sup>. The layer thickness was identified by optical contrast and PL emission energy. The MoS<sub>2</sub>/WSe<sub>2</sub> heterobilayers were stacked by aligning the long straight edges of the TMD flakes and stacking them together on the PDMS stamp. The twist angles are determined by analyzing the straight edges of the stacked heterobilayers in optical microscope images, as reported in previous works<sup>30,31</sup>. The measured twist angle can be correlated to the second harmonic generation (SHG) measurements and moiré pattern measurements by AFM (see Note S4). The length of the straight edges affects the twist angle's accuracy, and consequently, the IX energy fluctuates for a certain twist angle (especially at a twist angle of  $-0.5^\circ$ , see Fig. 1e). The heterobilayers used for AFM measurements were transferred to hBN flakes by the PDMS method and the stacked heterostructures were cleaned by I165 remover.

The cavities were fabricated on a commercial silicon-on-insulator (SOI) wafer with a 220 nm silicon layer and 2  $\mu$ m sacrificial silicon dioxide layer (SOITEC). A 180 nm layer of e-beam resist (CSAR AR-P6200) was prepared, followed by an electron beam lithography process (JBX-9500FSZ, JEOL). After development, the cavity was created via an inductively coupled plasma dry-etching process. The residual resist was finally dissolved in I165 solvent. The hBN thin films were exfoliated onto a SiO<sub>2</sub>/Si substrate for encapsulation. The bottom hBN layer was thinner than 10 nm for good coupling between moiré IXs and the cavity mode. The hBN-encapsulated MoS<sub>2</sub>/WSe<sub>2</sub> heterostructures were assembled and transferred to the cavities using the polymer-based dry-transfer method<sup>52</sup>.

### Optical measurements

All measurements were performed at room temperature. For the PL measurements, a 637 nm CW laser diode was used to pump the devices. A 50x objective lens with a numerical aperture (NA) of 0.65 (LCPLN50XIR, Olympus) was used for excitation and collection, yielding a laser spot size of  $\sim 1.5 \mu$ m. The laser light was blocked through longpass spectral filters, and the PL signals were sent to a Czerny-Turner monochromator (SR500i, Andor) with a cooled InGaAs 1D-array camera (DU491A-1.7, Andor). A 150 grooves/mm grating is used for the wide-range PL and RC spectra from MoS<sub>2</sub>/WSe<sub>2</sub> heterobilayers. Regarding the characterization of the cavity mode, a 1200 grooves/mm grating ( $\sim 0.1$  nm) was also used for better resolution.

In MoS<sub>2</sub>/WSe<sub>2</sub> heterobilayers, the quenched PL of intralayer excitons prevents one from using it for investigating moiré effects. Hence exciton absorption is measured instead to characterize the intralayer excitons. Regarding a heterobilayer on a transparent substrate (PDMS), the excitonic absorption is proportional to the reflection contrast (RC) that is defined as  $RC = (R_{sam} - R_{sub})/R_{sub}$ <sup>53</sup>, where  $R_{sam}$  and  $R_{sub}$  are the reflection from the sample and the substrate, respectively. Thus we capture the exciton resonances by performing RC spectroscopy with a white light source (SuperK Compact).

The time-resolved PL measurements were performed using a time-correlated single-photon counting (TCSPC) technique with a time tagger. We excited the device with a 640 nm pulsed laser (LDH-IB-640-B, PicoQuant) with a pulse width of  $< 90$  ps and a repetition rate of 10 MHz. The signals with wavelengths longer than 900 nm were sent to a single-photon detector (id220-FR, IDQ) by single-mode fiber coupling. Bandpass filters were used to measure the exciton lifetimes of different IX states.

Polarization-dependent SHG measurements were used to determine the twist angles of heterobilayers and were carried out with an

excitation wavelength of 960 nm (repetition rate 2 kHz) from an amplified Ti:sapphire femtosecond laser system (Spectra-Physics Solstice Ace). The polarization orientation of the excitation beam was tailored by rotating a half-wave plate (HWP). The laser light after the HWP was focused onto the sample by a 40x objective lens (NA = 0.75, Nikon). The transmitted SHG signal was collected by another 40x objective lens (NA = 0.5, Nikon), and passed through a linear polarizer. A 700 nm short-pass filter was placed after the polarizer to cut off the excitation beam. The final signal was detected by a photomultiplier tube (PMT) (Hamamatsu). The SHG measurements correlated the twist angle with IX energy (Fig. S13).

### AFM measurements

To obtain quantitative information about the surface topography, an AFM investigation has been carried out using a Bruker ICON AFM in Peak Force Quantitative NanoMechanics mode (PFQNM). In Peak Force mode, the force curves at each pixel are measured, and the peak force is used as the setpoint for the imaging feedback signal. The tip-surface distance in the PFQNM AFM is similar to contact AFM, thus enhancing the lateral resolution of imaging. In addition, PFQNM AFM allows quantitative determination of nano-mechanical properties of the surface from an analysis of force curves. We used Bruker ScanAsyst-Air-HR probes for the imaging. The probe has a nominal radius of 2 nm and a spring constant of 0.4 N/m. The reduced Young's modulus  $E$  is obtained from the fitting of the retraction force curve using the Derjaguin, Muller, Toropov (DMT) model of adhesion of solids<sup>54</sup>.

### Numerical simulation

The topological photonic nanobeam cavity that we adopted was first proposed in ref. 48. We retained a SiO<sub>2</sub> layer to support silicon nanobeams as our previous design<sup>46</sup>, which was mechanically robust for the 2D material transfer process and was preferable for efficient heat dissipation. We optimized the cavity mode and parameters to reach a desired resonant wavelength using the finite-difference time-domain method (Lumerical, Ansys). The detailed structure parameters of the cavities are shown in Fig. S14.

### Data availability

The data generated in this study and supporting the manuscript figures including those in the Supplementary Information have been deposited in the Zenodo database <https://doi.org/10.5281/zenodo.13629284>.

## References

- Kennes, D. M. et al. Moiré heterostructures as a condensed-matter quantum simulator. *Nat. Phys.* **17**, 155–163 (2021).
- Wilson, N. P., Yao, W., Shan, J. & Xu, X. Excitons and emergent quantum phenomena in stacked 2D semiconductors. *Nature* **599**, 383–392 (2021).
- Regan, E. C. et al. Emerging exciton physics in transition metal dichalcogenide heterobilayers. *Nat. Rev. Mater.* **7**, 778–795 (2022).
- Yan, X. et al. Moiré synaptic transistor with room-temperature neuromorphic functionality. *Nature* **624**, 551–556 (2023).
- Bistritzer, R. & MacDonald, A. H. Moiré bands in twisted double-layer graphene. *Proc. Natl Acad. Sci. USA* **108**, 12233–12237 (2011).
- Cao, Y. et al. Unconventional superconductivity in magic-angle graphene superlattices. *Nature* **556**, 43–50 (2018).
- Du, L. et al. Moiré photonics and optoelectronics. *Science* **379**, eadg0014 (2023).
- Rivera, P. et al. Interlayer valley excitons in heterobilayers of transition metal dichalcogenides. *Nat. Nanotechnol.* **13**, 1004–1015 (2018).
- Liu, Y. et al. Interlayer excitons in transition metal dichalcogenide semiconductors for 2D optoelectronics. *Adv. Mater.* **34**, 2107138 (2022).



10. Liu, Y. et al. Room temperature nanocavity laser with interlayer excitons in 2D heterostructures. *Sci. Adv.* **5**, eaav4506 (2019).
11. Paik, E. Y. et al. Interlayer exciton laser of extended spatial coherence in atomically thin heterostructures. *Nature* **576**, 80–84 (2019).
12. Qian, C. et al. Lasing of moiré trapped mose2/wse2 interlayer excitons coupled to a nanocavity. *Sci. Adv.* **10**, eadk6359 (2024).
13. He, F. et al. Moiré patterns in 2D materials: a review. *ACS Nano* **15**, 5944–5958 (2021).
14. Li, H. et al. Imaging moiré flat bands in three-dimensional reconstructed WSe<sub>2</sub>/WS<sub>2</sub> superlattices. *Nat. Mater.* **20**, 945–950 (2021).
15. Susarla, S. et al. Hyperspectral imaging of exciton confinement within a moiré unit cell with a subnanometer electron probe. *Science* **378**, 1235–1239 (2022).
16. Hagel, J., Brem, S., Pineiro, J. A. & Malic, E. Impact of atomic reconstruction on optical spectra of twisted tmd homobilayers. *Phys. Rev. Mater.* **8**, 034001 (2024).
17. Yu, H., Liu, G.-B., Tang, J., Xu, X. & Yao, W. Moiré excitons: From programmable quantum emitter arrays to spin-orbit-coupled artificial lattices. *Sci. Adv.* **3**, e1701696 (2017).
18. Tran, K. et al. Evidence for moiré excitons in van der Waals heterostructures. *Nature* **567**, 71–75 (2019).
19. Jin, C. et al. Observation of moiré excitons in WSe<sub>2</sub>/WS<sub>2</sub> heterostructure superlattices. *Nature* **567**, 76–80 (2019).
20. Seyler, K. L. et al. Signatures of moiré-trapped valley excitons in MoSe<sub>2</sub>/WSe<sub>2</sub> heterobilayers. *Nature* **567**, 66–70 (2019).
21. Alexeev, E. M. et al. Resonantly hybridized excitons in moiré superlattices in van der Waals heterostructures. *Nature* **567**, 81–86 (2019).
22. Karni, O. et al. Structure of the moiré exciton captured by imaging its electron and hole. *Nature* **603**, 247–252 (2022).
23. Schmitt, D. et al. Formation of moiré interlayer excitons in space and time. *Nature* **608**, 499–503 (2022).
24. Merkl, P. et al. Ultrafast transition between exciton phases in van der Waals heterostructures. *Nat. Mater.* **18**, 691–696 (2019).
25. Jiang, Y., Chen, S., Zheng, W., Zheng, B. & Pan, A. Interlayer exciton formation, relaxation, and transport in TMD van der Waals heterostructures. *Light. Sci. Appl.* **10**, 72 (2021).
26. Tan, Q., Rasmita, A., Zhang, Z., Novoselov, K. & Gao, W. Signature of cascade transitions between interlayer excitons in a moiré superlattice. *Phys. Rev. Lett.* **129**, 247401 (2022).
27. Sun, X. et al. Enhanced interactions of interlayer excitons in free-standing heterobilayers. *Nature* **610**, 478–484 (2022).
28. Karni, O. et al. Infrared interlayer exciton emission in MoS<sub>2</sub>/WSe<sub>2</sub> heterostructures. *Phys. Rev. Lett.* **123**, 247402 (2019).
29. Tan, Q. et al. Layer-engineered interlayer excitons. *Sci. Adv.* **7**, eabh0863 (2021).
30. Baek, H. et al. Highly energy-tunable quantum light from moiré-trapped excitons. *Sci. Adv.* **6**, eaba8526 (2020).
31. Fang, H. et al. Localization and interaction of interlayer excitons in MoSe<sub>2</sub>/WSe<sub>2</sub> heterobilayers. *Nat. Commun.* **14**, 6910 (2023).
32. Chatterjee, S. et al. Harmonic to anharmonic tuning of moiré potential leading to unconventional stark effect and giant dipolar repulsion in WS<sub>2</sub>/WSe<sub>2</sub> heterobilayer. *Nat. Commun.* **14**, 4679 (2023).
33. Brem, S. & Malic, E. Bosonic delocalization of dipolar moiré excitons. *Nano Lett.* **23**, 4627–4633 (2023).
34. Zhang, L. et al. Van der Waals heterostructure polaritons with moiré-induced nonlinearity. *Nature* **591**, 61–65 (2021).
35. Barré, E. et al. Optical absorption of interlayer excitons in transition-metal dichalcogenide heterostructures. *Science* **376**, 406–410 (2022).
36. Kolobov, A. V. & Tominaga, J. *Two-Dimensional Transition-Metal Dichalcogenides* 1st edn, Vol. 239 (Springer, 2016).
37. Carrascoso, F., Frisenda, R. & Castellanos-Gomez, A. Biaxial versus uniaxial strain tuning of single-layer MoS<sub>2</sub>. *Nano Mater. Sci.* **4**, 44–51 (2022).
38. Van Winkle, M. et al. Rotational and dilational reconstruction in transition metal dichalcogenide moiré bilayers. *Nat. Commun.* **14**, 2989 (2023).
39. Woods, C. et al. Commensurate-incommensurate transition in graphene on hexagonal boron nitride. *Nat. Phys.* **10**, 451–456 (2014).
40. Li, H. et al. Imaging moiré excited states with photocurrent tunnelling microscopy. *Nat. Mater.* **23**, 633–638 (2024).
41. Klimov, V. I. et al. Single-exciton optical gain in semiconductor nanocrystals. *Nature* **447**, 441–446 (2007).
42. Wang, Z. et al. Evidence of high-temperature exciton condensation in two-dimensional atomic double layers. *Nature* **574**, 76–80 (2019).
43. Choi, J. et al. Twist angle-dependent interlayer exciton lifetimes in van der Waals heterostructures. *Phys. Rev. Lett.* **126**, 047401 (2021).
44. Sun, D. et al. Observation of rapid exciton–exciton annihilation in monolayer molybdenum disulfide. *Nano Lett.* **14**, 5625–5629 (2014).
45. Amani, M. et al. Near-unity photoluminescence quantum yield in MoS<sub>2</sub>. *Science* **350**, 1065–1068 (2015).
46. Fang, H. et al. Laser-like emission from a sandwiched MoTe<sub>2</sub> heterostructure on a silicon single-mode resonator. *Adv. Opt. Mater.* **7**, 1900538 (2019).
47. Bandres, M. A. et al. Topological insulator laser: experiments. *Science* **359**, eaar4005 (2018).
48. Ota, Y., Katsumi, R., Watanabe, K., Iwamoto, S. & Arakawa, Y. Topological photonic crystal nanocavity laser. *Commun. Phys.* **1**, 86 (2018).
49. Wen, W., Wu, L. & Yu, T. Excitonic lasers in atomically thin 2D semiconductors. *ACS Mater. Lett.* **2**, 1328–1342 (2020).
50. Kreinberg, S. et al. Emission from quantum-dot high-β microcavities: transition from spontaneous emission to lasing and the effects of superradiant emitter coupling. *Light. Sci. Appl.* **6**, e17030 (2017).
51. Castellanos-Gomez, A. et al. Deterministic transfer of two-dimensional materials by all-dry viscoelastic stamping. *2D Mater.* **1**, 011002 (2014).
52. Zomer, P., Guimarães, M., Brant, J., Tombros, N. & Van Wees, B. Fast pick up technique for high quality heterostructures of bilayer graphene and hexagonal boron nitride. *Appl. Phys. Lett.* **105**, 013101 (2014).
53. Zhao, W. et al. Evolution of electronic structure in atomically thin sheets of WS<sub>2</sub> and WSe<sub>2</sub>. *ACS Nano* **7**, 791–797 (2013).
54. Derjaguin, B. V., Muller, V. M. & Toporov, Y. P. Effect of contact deformations on the adhesion of particles. *J. Colloid Interface Sci.* **53**, 314–326 (1975).

## Acknowledgements

We thank Witlef Wieczorek for helpful discussions. This work was partially funded by the Danish National Research Foundation through the Center for Nanostructured Graphene (project no. DNRF103) and through NanoPhoton - Center for Nanophotonics (project no. DNRF147). N.S. acknowledges the support from the VILLUM FONDEN (project no. 00028233). Q.L. and S.X. acknowledge the support from the Independent Research Fund Denmark (project no. 9041-00333B and 2032-00351B), Direktør Ib Henriksens Fond, and Brødrene Hartmanns Fond. N.S. and M.W. acknowledge the support from the Independent Research Fund Denmark, Natural Sciences (project no. 0135-00403B). H.F. acknowledges support by the Olle Engkvists stiftelse, the Carl Tryggers stiftelse, and Chalmers Excellence Initiative Nano. J.L. and H.F. acknowledge the support from the National Natural Science Foundation of China (project no. 11974436). Y.L. acknowledges the support from A\*STAR Career Development Fund - Seed Projects (C222812008). E.M. acknowledges support from the Deutsche Forschungsgemeinschaft (DFG) via SFB 1083 and regular project 524612380. Y.Z. and Z.S. acknowledge the support from Horizon Europe (HORIZON) Project: ChirLog (101067269), the Academy of Finland (grants 314810, 333982, 336144, 336818, 352780, 360411, and 353364), Academy of Finland

Flagship Programme (320167, PREIN), the EU H2020-MSCA-RISE-872049 (IPN-Bio), and ERC Advanced Grant (834742).

## Author contributions

H.F. and S.X. conceived and supervised the project. Q.L. and H.F. designed the device. Q.L., J.L., and Y.L. fabricated the devices. Q.L. and H.F. performed PL characterizations. A.K. and H.F. performed the AFM measurements. Y.Z. performed the polarization-resolved SHG measurements. Q.L., H.F., and M.F. performed lifetime measurements. Q.L. and H.F. carried out simulations of the topological cavities. J.H., S.B., and E.M. helped analyze the experimental data. Q.L., H.F., Z.S., M.W., N.S., and S.X. analyzed the data. All authors contributed to the discussion and writing of the manuscript.

## Competing interests

The authors declare no competing interests.

## Additional information

**Supplementary information** The online version contains supplementary material available at <https://doi.org/10.1038/s41467-024-53083-x>.

**Correspondence** and requests for materials should be addressed to Hanlin Fang or Sanshui Xiao.

**Reprints and permissions information** is available at <http://www.nature.com/reprints>

**Publisher's note** Springer Nature remains neutral with regard to jurisdictional claims in published maps and institutional affiliations.

**Open Access** This article is licensed under a Creative Commons Attribution-NonCommercial-NoDerivatives 4.0 International License, which permits any non-commercial use, sharing, distribution and reproduction in any medium or format, as long as you give appropriate credit to the original author(s) and the source, provide a link to the Creative Commons licence, and indicate if you modified the licensed material. You do not have permission under this licence to share adapted material derived from this article or parts of it. The images or other third party material in this article are included in the article's Creative Commons licence, unless indicated otherwise in a credit line to the material. If material is not included in the article's Creative Commons licence and your intended use is not permitted by statutory regulation or exceeds the permitted use, you will need to obtain permission directly from the copyright holder. To view a copy of this licence, visit <http://creativecommons.org/licenses/by-nc-nd/4.0/>.

© The Author(s) 2024